ECCOMAS Congress 2016
VII European Congress on Computational Methods in Applied Sciences and Engineering
M. Papadrakakis, V. Papadopoulos, G. Stefanou, V. Plevris (eds.)
Crete Island, Greece, 5–10 June 2016

MODELING OF EXCITATION OF CONTROLLING DISTURBANCES IN SWEPT WING BOUNDARY LAYER BY MEANS OF PLASMA ACTUATORS

Sergey L. Chernyshev [1], **Andrey Ph. Kiselev** [1], **and Aleksandr P. Kuryachii** [1]

[1] Central Aerohydrodynamic Institute (TsAGI)
1, Zhukovsky str., Zhukovsky, 140180 Moscow region, Russia
e-mail: aleksandr.kuryachiy@tsagi.ru

Keywords: Swept Wing, Cross-Flow-Type Instability, Plasma Actuator.

Abstract. *Two variants of multiple dielectric barrier discharge (DBD) actuator are proposed for generation the variable amplitude forced modes in thin boundary layer near a swept wing leading edge with the aim to cancel the critical cross-flow-type instability modes resulting in laminar-turbulent transition. Numerical simulation of the excitation of stationary forced modes by DBD-actuators in compressible 3D boundary layer on an infinite span swept wing at typical cruise flight conditions has been executed to estimate the possibility of the proposed method of transition control. Spanwise periodic localized volumetric force and heat impact on boundary layer flow at realistic physical parameters of DBD has been considered. It is shown that DBD-actuators generate three rows of pairs of counter-rotating vortices one above another along local inviscid streamline.*

1 INTRODUCTION

Development of innovative aerodynamic technologies for a more effective, environmentally friendly air transport system remains in the centre of attention of the aeronautical community. Cruise drag reduction is one of the main goals of these developments [1]. The viscous drag contributes about a half of the total cruise drag of modern airplanes. A delaying laminar-to-turbulent transition in boundary layer on aerodynamic surfaces is one of the effective methods of viscous drag reduction. Laminar-to-turbulent transition on a swept wing of typical subsonic airplane in cruise flight is caused, as a rule, by cross-flow-type instability modes, which evolve as a pairs of stationary counter-rotating vortices, whose axes are closely aligned with local inviscid streamlines [2]. Therefore any method of suppression of these instability modes would be a key to solution the problem of a swept wing drag reduction, if this method is constructive reliable and energy acceptable.

Saric et al. [3] have shown that the linear predicted most unstable mode leading to transition (termed the critical mode) could be suppressed, thereby delaying transition, by distributing spanwise-periodic discrete surface roughness elements (DREs) near the wing leading edge at spacing approximately equal to one-half of the spanwise wavelength of the critical mode. The micron-high roughness elements produce a rapid growth of the forced controlling mode and then its decay. This forced mode suppresses the critical mode, thus delaying transition beyond the natural location that would occur in the absence of any artificial roughness.

The three principal types of DREs include: appliqué, pneumatic, and dielectric barrier discharge (DBD) actuators [4]. Note, that DREs have to be placed near the neutral stability point rather upstream. Both Reynolds number and the angle of attack can change during cruise flight. Different Reynolds number produce different wavelengths of the critical mode and different angles of attack produce different positions of neutral stability point. Therefore some wavelength and chord-position variability is required in any DREs system. It is evident that appliqué DREs don't satisfy this requirement. Pneumatically driven actuator proposed in [5] is capable of producing variable height of surface roughness thereby ensuring variable amplitude of the exited controlling mode. Different amplitude can be fitted to different neutral stability point position. Main disadvantages of the pneumatic variable roughness actuator [5] consist in 1) difficulty to produce controlling mode with very short wavelength and 2) high probability of destruction of thin flexible tape covering orifices by solid or ice particles.

Dielectric barrier discharge actuators with streamwise oriented external electrodes have been used for generation of near-surface streamwise vortices first in [6] and then have been investigated in details in [7, 8]. Sandwich DBD-actuator with an additional control electrode has been considered in [9]. But long external electrodes placed parallel to the free stream direction are necessary to generate strong enough streamwise vortices in these configurations of DBD actuators. Streamwise vortices can be generated also in DBD actuators with serrated [10] or serpentine [11] external electrodes which can have small extension in streamwise direction. But these configurations seem to be too power-consuming because the discharge takes place along the whole external electrode in spanwise direction.

2 MULTIPLE DIELECTRIC BARRIER DISCHARGE ACTUATORS

Simple design of multi-DBD actuator recently proposed at TsAGI permits to generate the variable forced modes in thin boundary layer near a swept wing leading edge. The mode intensity can be adjusted to varying position of neutral stability point by changing voltage or frequency of DBD. Unfortunately this design does not permit to vary the spanwise wavelength of the generated modes. Main advantages of the proposed DBD actuator consist

in low power consumption and the possibility of significant miniaturization for generation short-wave modes.

Two variants of multi-DBD actuator are presented on Fig. 1. Here *1* is the wing skin which must be electricity-conductive and equipotential in accordance with electrostatic safety requirements, *2* is the dielectric insert, *3* is the buried accelerating electrode, *4* is the exposed electrode in the form of a comb, *5* is the high voltage power supply, *6* are the regions of DBD. It is supposed that the external electrode *4* is flush mounted and the tips of the comb teeth are placed at some distance upstream from the position of neutral stability point. The spanwise period of the teeth λ is equal to the wavelength of the exited controlling mode. The exposed electrode *4* is electrically linked with the wing skin *1* and one output of the power supply *5* is connected with the skin. Other output of the power supply is connected with the buried electrode *3*. One edge of the buried electrode *3* is arranged directly beneath the tips of the comb teeth *4*. The other edge of the buried electrode is distant enough from the skin to avoid the discharge ignition near the skin border.

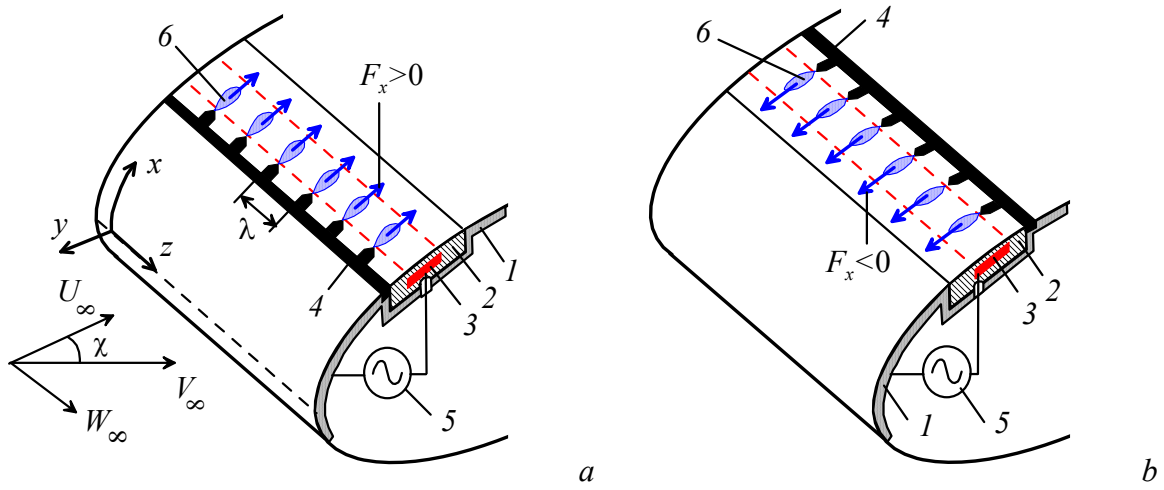

Figure 1: Design of multi-DBD actuators.

The time averaged volumetric force arising in the discharge regions *6* has two components. The main component F_x is directed along a wing surface perpendicular to a wing leading edge, i. e. along the *x*-axis, and the other component is directed perpendicular to a wing surface. The spanwise component of the generated force can be neglected. The *x*-component of the volumetric force is directed downstream ($F_x > 0$) in the variant 1 shown on Fig. 1, *a* and upstream ($F_x < 0$) in the variant 2 shown on Fig. 1, *b*. Volumetric force impact directed perpendicular to the leading edge in both variants results in a vorticity generation both in *x*- and *z*-direction and, as a result, a formation of vortex system aligned with external streamline.

3 CHARACTERISTICS OF CROSS-FLOW-TYPE INSTABILITY

The possibility of multi-DBD actuator to generate the streamwise vortices is estimated on the example of a subsonic flow over infinite span swept wing with sweep angle of $\chi = 30^o$. The static pressure $p_\infty = 2.6 \cdot 10^4$ Pa, the air temperature $T_\infty = 223$ K corresponding to the flight altitude of 10 km, and Mach number $M_\infty = 0.8$ are taken as the main free-stream parameters. They determine other flow parameters necessary for inviscid and boundary layer calculations: the flow velocity $V_\infty = 240$ m/s, the air density $\rho_\infty = 0.41$ kg/m^3, the dynamic viscosity coefficient $\mu_\infty = 1.33 \cdot 10^{-5}$ kg/(m·s).

The external boundary conditions for calculations of the compressible boundary layer have been obtained from a calculation of 2D inviscid flow over experimental LV6 DLR airfoil at zero angle of attack on the base of the Euler equations. The boundary layer flow in the vicinity of a wing leading edge is characterized by Reynolds number $\mathrm{Re}_l = \rho_\infty V_\infty l/\mu_\infty$ determined by streamwise length $l = V_\infty/[du_e(0)/dx]$ which is equal approximately to a half radius of the leading edge curvature, where u_e is the x-component of the external velocity obtained from inviscid calculation. The airfoil chord length L normal to a leading edge is related with the characteristic length l as $L = l\, du_e^{/}(0)/dx^{/}$, where the dimensionless velocity $u_e^{/}$ and the coordinate $x^{/}$ are measured in $V_\infty\cos\chi$ and L, respectively. According to executed 2D inviscid flow calculation, $du_e^{/}(0)/dx^{/} = 107.7$. The value $l = 0.03$ m was taken in the present estimations, hence, the airfoil chord length equals $L = 3.23$ m. The specified above free-stream parameters and characteristic length l determine the value of the Reynolds number $\mathrm{Re}_l = 2.03\cdot10^5$ and the estimation for the boundary layer thickness on the critical line of the wing leading edge $\delta_0 \approx 5\mathrm{Re}_l^{-1/2} l \approx 0.33$ mm.

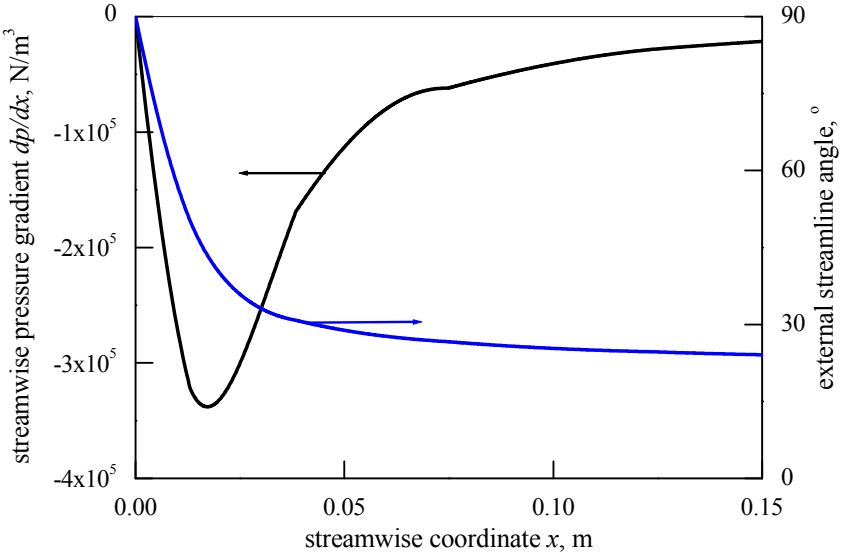

Figure 2: Streamwise distributions of the static pressure gradient and the angle of the inviscid streamline.

The inviscid flow over LV6 airfoil is characterized by very short part (less than 5% of the chord length) of strong flow acceleration as it is seen on Fig. 2. Here the static pressure gradient along a wing surface perpendicular to the leading edge and the angle ψ between the x-axis and the external inviscid streamline are shown.

The compressible boundary layer flow on a swept wing is described by the velocity components u, v, w, the static pressure p, the air density ρ, the static enthalpy $h = c_p T$ which are governed by the following system of equations and boundary conditions in Cartesian coordinate system shown on Fig. 1, *a*:

$$\frac{\partial(\rho u)}{\partial x} + \frac{\partial(\rho v)}{\partial y} + \frac{\partial(\rho w)}{\partial z} = 0$$

$$\rho u\frac{\partial u}{\partial x} + \rho v\frac{\partial u}{\partial y} + \rho w\frac{\partial u}{\partial z} = \frac{\partial}{\partial y}\left(\mu\frac{\partial u}{\partial y}\right) - \frac{dp}{dx} + F_x$$

$$\rho u\frac{\partial w}{\partial x} + \rho v\frac{\partial w}{\partial y} + \rho w\frac{\partial w}{\partial z} = \frac{\partial}{\partial y}\left(\mu\frac{\partial w}{\partial y}\right)$$

$$\rho u\frac{\partial h}{\partial x}+\rho v\frac{\partial h}{\partial y}+\rho w\frac{\partial h}{\partial z}=\frac{\partial}{\partial y}\left(\frac{\mu}{\mathrm{Pr}}\frac{\partial h}{\partial y}\right)+u\frac{dp}{dx}+\mu\left[\left(\frac{\partial u}{\partial y}\right)^2+\left(\frac{\partial w}{\partial y}\right)^2\right]+Q$$

$$\rho=\frac{\gamma}{\gamma-1}\frac{p}{h} \tag{1}$$

$$y=0:\ u=v=w=\partial h/\partial y=0;\quad y=y_e:\ u=u_e,\ w=w_e,\ h=h_e$$

$$x=0:\quad u=xU(y),\quad \rho U+\frac{d(\rho v)}{dy}=0,\quad \frac{d}{dy}\left(\mu\frac{dU}{dy}\right)-\rho v\frac{dU}{dy}-\rho U^2=0$$

$$\frac{d}{dy}\left(\mu\frac{dw}{dy}\right)-\rho v\frac{dw}{dy}=0,\quad \frac{d}{dy}\left(\frac{\mu}{\mathrm{Pr}}\frac{dh}{dy}\right)-\rho v\frac{dh}{dy}+\mu\left(\frac{dw}{dy}\right)^2=0$$

$$w_e=V_\infty\sin\chi,\quad h_e=h_\infty+0.5\left(V_\infty^2-u_e^2-w_e^2\right),\quad p_e=p_\infty\left(h_e/h_\infty\right)^{\gamma/(\gamma-1)}$$

$$\mu(T)=1.47\cdot10^{-6}\frac{T^{3/2}}{T+114},\quad \gamma=1.4,\ \mathrm{Pr}=0.72$$

Here F_x and Q are the spatial distributions of the time averaged streamwise volumetric force and Joule dissipation generated in discharge near every tooth of actuator and determined in analytical form below. The subscript e denotes the values of functions on the external boundary y_e of the boundary layer. The wing surface is supposed to be heat-insulated.

The gas velocity vector at some point inside a boundary layer can be represented by u- and w-components or by main-flow V_{MF} and cross-flow V_{CF} components related by the following expressions:

$$V_{MF}=u\cos\psi+w\sin\psi,\quad V_{CF}=u\sin\psi-w\cos\psi,\quad \mathrm{tg}\,\psi=w_e/u_e,\quad w_e=V_\infty\sin\chi \tag{2}$$

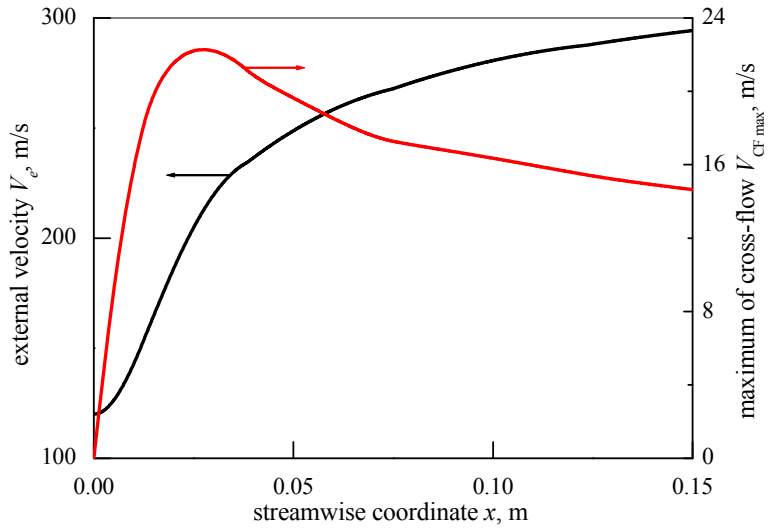

Figure 3: Streamwise distributions of the maximal main-flow and cross-flow velocities.

The streamwise distributions of the maximal main-flow velocity V_e achieving on the outer border of the boundary layer and the maximal cross-flow velocity $V_{CF\max}$ calculated without volumetric force and heat sources are presented on Fig. 3. It is seen that strong flow

acceleration results in very intensive cross-flow with maximal value of the cross-flow velocity achieving about 10% of the free stream velocity.

The stability characteristics of the considered boundary layer flow have been calculated in [12] in the framework of the linear stability equation system of Dunn-Lin [13]. Only steady cross-flow-type disturbances were considered. The well-known e^N-method was used to estimate the position of laminar-turbulent transition [2]. So the disturbances of all flow functions q and the N factor were defined as follows:

$$q = q^*(y)\exp(-\alpha_i x)\exp[i(\alpha_r x + \beta z)], \quad N(x) = -\int_{x_0}^{x} \alpha_i dx \tag{3}$$

Here q^* is the complex eigenfunction, $\alpha = \alpha_r + i\alpha_i$ is the complex eigenvalue, α_r and β represent the wave number components in x- and z-directions, α_i represents increment of spatial growth ($\alpha_i < 0$) or decrement of decay ($\alpha_i > 0$) of disturbances, x_0 is the initial coordinate where α_i obtains negative value, i.e. the disturbance becomes unstable. The so-called fixed β strategy [2] was used for N factor computation. That is the streamwise distributions of eigenvalue α and N factor are calculated according to (5) for a set of fixed spanwise wave numbers β.

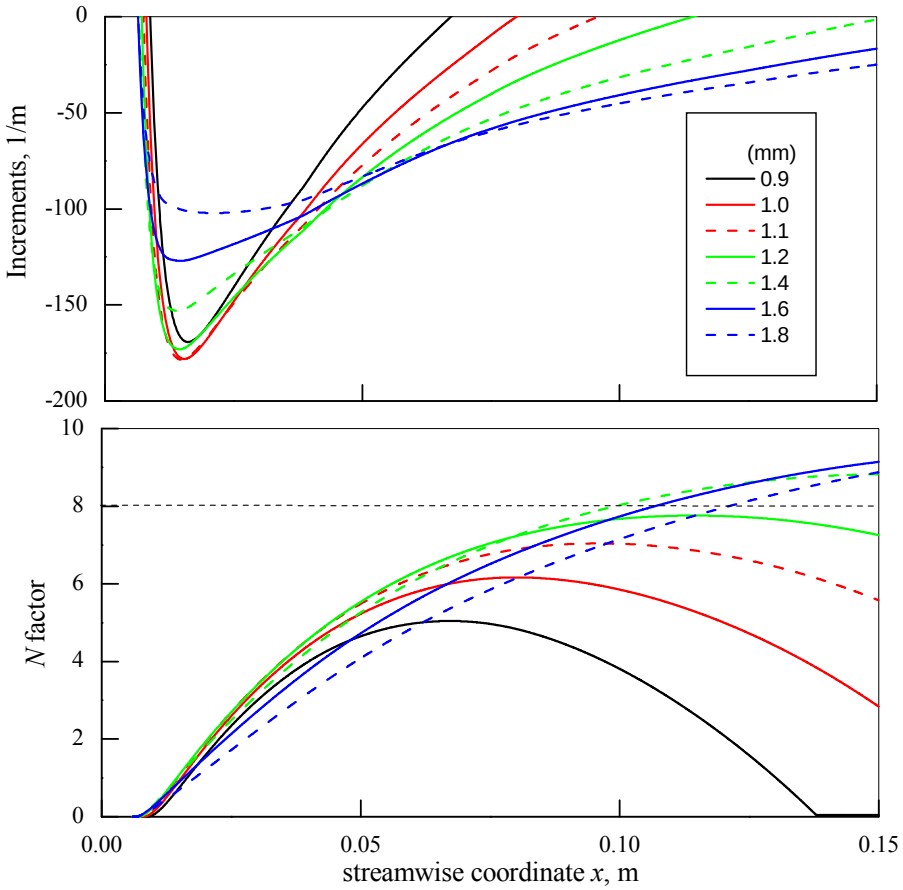

Figure 4: Streamwise distributions of increments of spatial growth and N factors for different spanwise wavelengths.

The mentioned above strong cross-flow in boundary layer results in a high flow instability. The calculated streamwise distributions of the increments of spatial growth of steady disturbances and N factors for different spanwise wavelength $\lambda = 2\pi/\beta$ in the range of 0.9-1.8

mm are shown on Fig. 4. The e^N-method implies that laminar-turbulent transition occurs when N factor for any spanwise wave number β (or corresponding wavelength λ) reaches some predefined value N_T. The position of the transition induced by steady cross-flow-type instability is estimated by $N_T = 8\text{-}10$ for the fixed β strategy [2]. According to lower Fig. 4, the disturbances with spanwise wavelengths $\lambda < 1.2$ mm are nonhazardous. The transition can be induced by disturbances with wavelengths $\lambda > 1.4$ mm at the distance $x_T \geq 0.1$ m from a critical line on the leading edge.

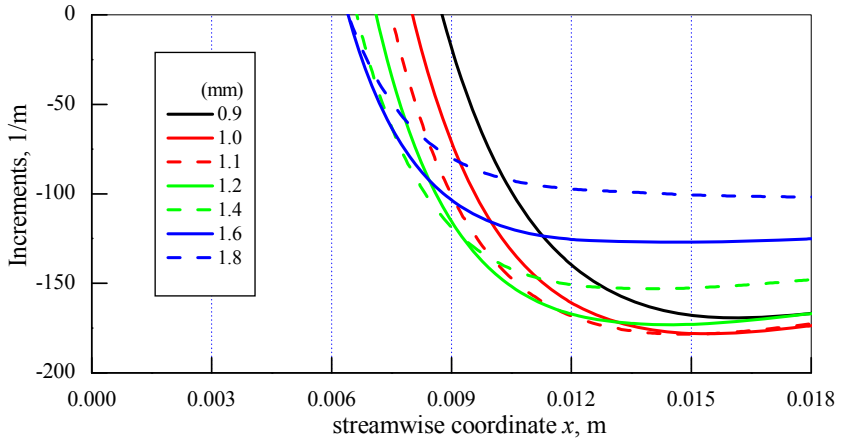

Figure 5: Distributions of increments of spatial growth in the vicinity of neutral point.

The disturbance with wavelengths $\lambda = 0.9$ mm seems to be an appropriate candidate for controlling forced mode to suppress the dangerous modes. This mode is amplified up to $x = 0.067$ m where the increments of dangerous modes attenuate appreciably, according to Fig. 4. The peculiarity of the considered particular case consists in the fact that short wave unstable modes arise downstream with respect to longer wave modes, as it is seen on Fig. 5 where the increments of the considered modes in the vicinity of neutral stability point are shown.

4 VORTICITY GENERATION BY IMPACT OF MILTI-DBD ACTUATOR

The impact of multi-DBD actuator on boundary layer flow is estimated in the framework of the system of equations and boundary conditions (1) for span-periodic flow. Numerical solution of the system (1) has been executed with the use of the expansion of all dependent variables and volumetric sources defined below in finite Fourier series and subsequent solution of the resulting 2D equation systems.

The spatial distributions of volumetric force and heat sources are taken in analytic form. The distribution of the force source in x-y plane for both positive F_+ and negative F_- force is described by the simple formula proposed in [14] and giving satisfactorily agreement with experimental data concerning the flow velocity induced by DBD actuators. The spanwise distribution is taken as a half of sine function, so the final expressions take the following form:

$$F_{\pm}(x,y,z) = F_t \frac{\pi}{2} \frac{x^{/} y^{/}}{x_0 y_0 z_0} \exp\left(\mp x^{/} - y^{/}\right) \sin\left(\pi z^{/}\right)$$

$$x^{/} = \left(x - x_{in}\right)/x_0, \quad y^{/} = y/y_0, \quad z^{/} = z/z_0, \quad 0 \leq y \leq y_e, \quad 0 \leq z \leq z_0 \qquad (4)$$

$$x_{in} \leq x \leq \infty \text{ for } F_+, \quad 0 \leq x \leq x_{in} \text{ for } F_-$$

Here F_t is the total source intensity in N, x_0 and y_0 are the coordinates of the distribution maximum (for F_+) or minimum (for F_-) in x-y plane, z_0 is the source size along a span, x_{in} is the coordinate of the tooth tip of the exposed electrode. It is supposed that the teeth tips are placed at same coordinate x_{in}= 6 mm, i.e. immediately in front of the neutral stability point, taking into account Fig. 5, in both variants of actuator shown on Fig. 1. The discharge regions propagate from x_{in} downstream in the variant 1 (F_+) or upstream in the variant 2 (F_-).

The spanwise period of multi-DBD actuator is equal to λ = 9 mm and the size of the force source along a span equals z_0= 4.5 mm. The following considerations have been taken into account at a choice of the other parameters of the distributions (4). The relation of the characteristic longitudinal to transversal sizes of the time averaged volumetric force distributions is estimated as 4:1 according to various experimental data [15-17]. The force distribution varies in the homothetic manner at variation the amplitude or the frequency of applied voltage [17]. The local maximum force density can reach about F_{max}= 10^4·N/m^3 [18].

The total force per one tooth of the exposed electrode is estimated according to (4) as $F_t = 2e^2 F_{max} x_0 y_0 z_0/\pi \approx 4.74\, F_{max} x_0 y_0 z_0$. The following characteristic sizes have been taken in calculations: x_0 = 0.4 mm, y_0 = 0.1 mm, hence F_t = 8.5·10^{-7}·N at $F_{max}\approx$ 10^4·N/m^3.

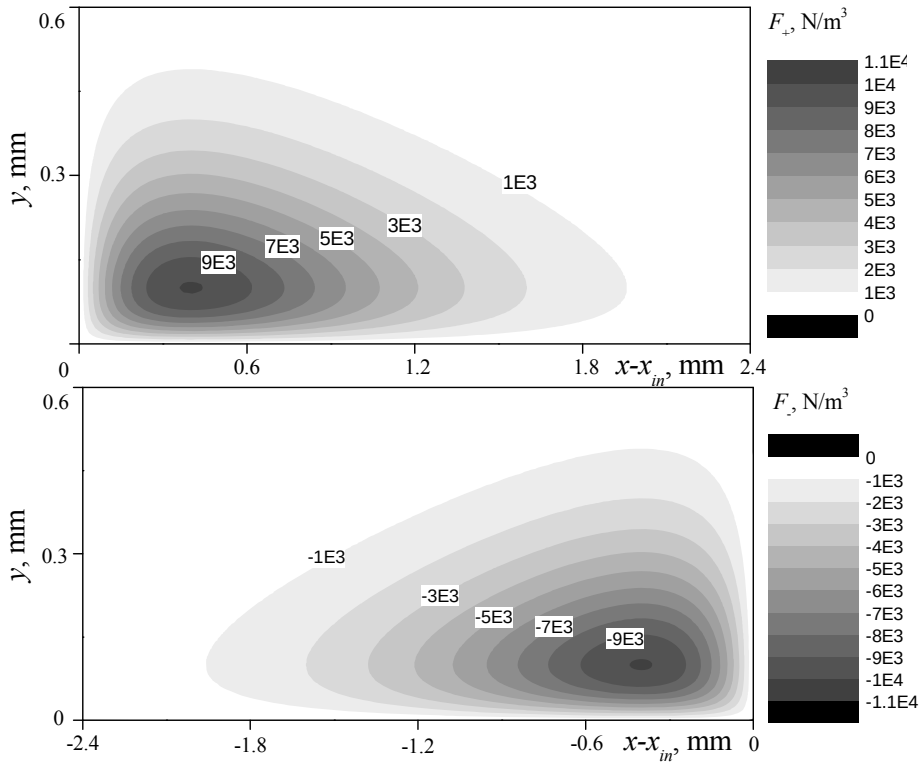

Figure 6: Spatial distributions of the volumetric force sources in x-y plane.

The spatial distributions of the positive and negative force sources in x-y plane at $z = 0.5z_0$ are shown on Fig. 6. It is seen that the vertical size of the sources slightly exceeds the boundary layer thickness on the critical line of the wing leading edge δ_0. The external boundary in the present calculations has been taken as y_e = 1.5 mm. The selected above parameters of the force distributions (4) can bee considered as ultimate for this specific case of boundary layer flow. Further increase in the source intensity would lead to its protrusion in external inviscid flow.

The distribution of the volumetric heat source has been taken in the analytic form approximately accounting for characteristic features of the Joule dissipation distribution in

DBD revealed in numerical simulation [12]. The heat sources in both variants of actuator are naturally positive and take the forms

$$Q_{\pm}(x,y,z) = \pm Q_t \frac{\pi}{2} \frac{x_q^{/}}{x_{q0} y_{q0} z_{q0}} \exp\left(\mp x_q^{/} - y_q^{/}\right) \sin\left(\pi z_q^{/}\right)$$
$$x_q^{/} = \left(x - x_{in}\right)/ x_{q0}, \quad y_q^{/} = y / y_{q0}, \quad z_q^{/} = z / z_{q0}, \quad 0 \le y \le y_e, \quad 0 \le z \le z_{q0} \qquad (5)$$
$$x_{in} \le x \le \infty \text{ for } Q_+, \quad 0 \le x \le x_{in} \text{ for } Q_-$$

The maximal value of heat release according to (5) is reached on the wing surface. The accepted energy efficiency of the actuator $E \equiv F_t/Q_t = 10^{-4}$ s/m corresponds to medium value of efficiency obtained in experiments [18]. The following parameters of the distributions (5) have been used in calculations: $x_{q0} = 0.2$ mm, $y_{q0} = 0.05$ mm, $z_{q0} = 4.5$ mm, $Q_t = 8.5 \cdot 10^{-3}$·W. The spatial distribution of the heat source Q_+ in x-y plane at $z = 0.5 z_0$ is shown on Fig. 7. The distribution of the heat source Q_- is reflection symmetric relative to coordinate x_{in}.

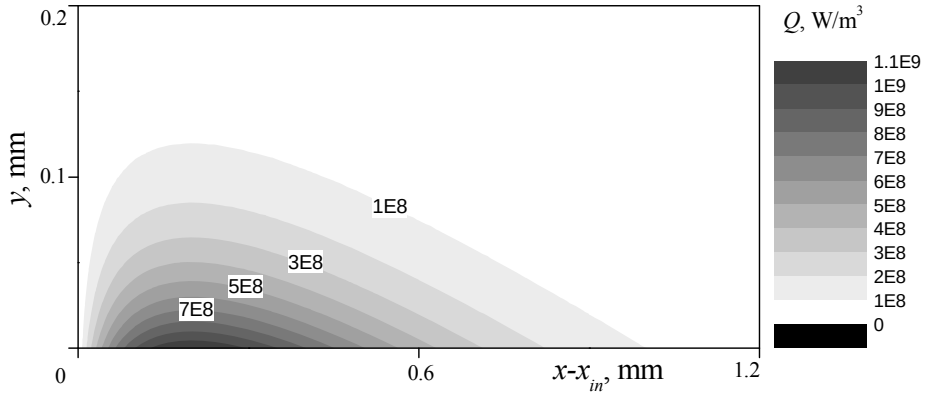

Figure 7: Spatial distribution of the volumetric heat source in x-y plane.

Volumetric force and heat impact of actuator results in span-periodic perturbation of the boundary layer velocity. Spanwise distribution of disturbances of the main-flow velocity component determined by formulas (2) at the distance $x = 6.3$ mm for variant 1 is shown on Fig. 8 as an example. The extremal values of the disturbances of the main-flow and cross-flow velocity components are presented on Fig. 9 both for combined force and heat impact (solid curves) and for only force impact (dashed curves). The effect of only force impact on the flow velocity is weak and the amplitude of the velocity disturbances is of the order of 10^{-2} m/s. The heat impact results in up to the order greater effect.

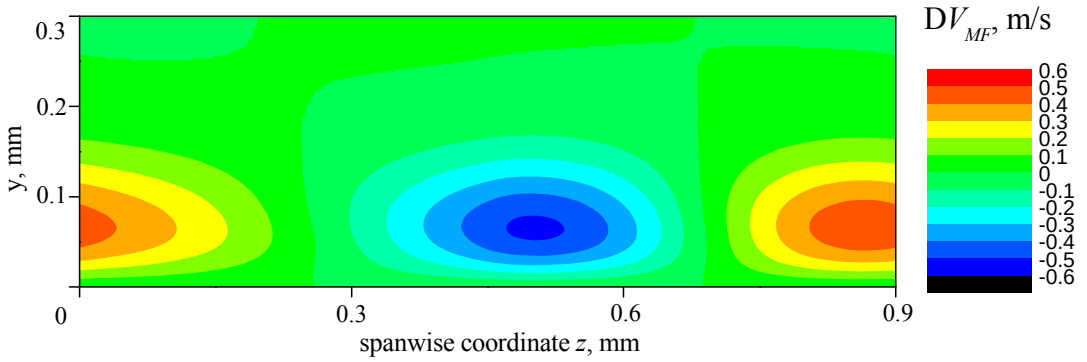

Figure 8: Distribution of main-flow velocity disturbances in z-y plane at $x = 6.3$ mm (variant 1).

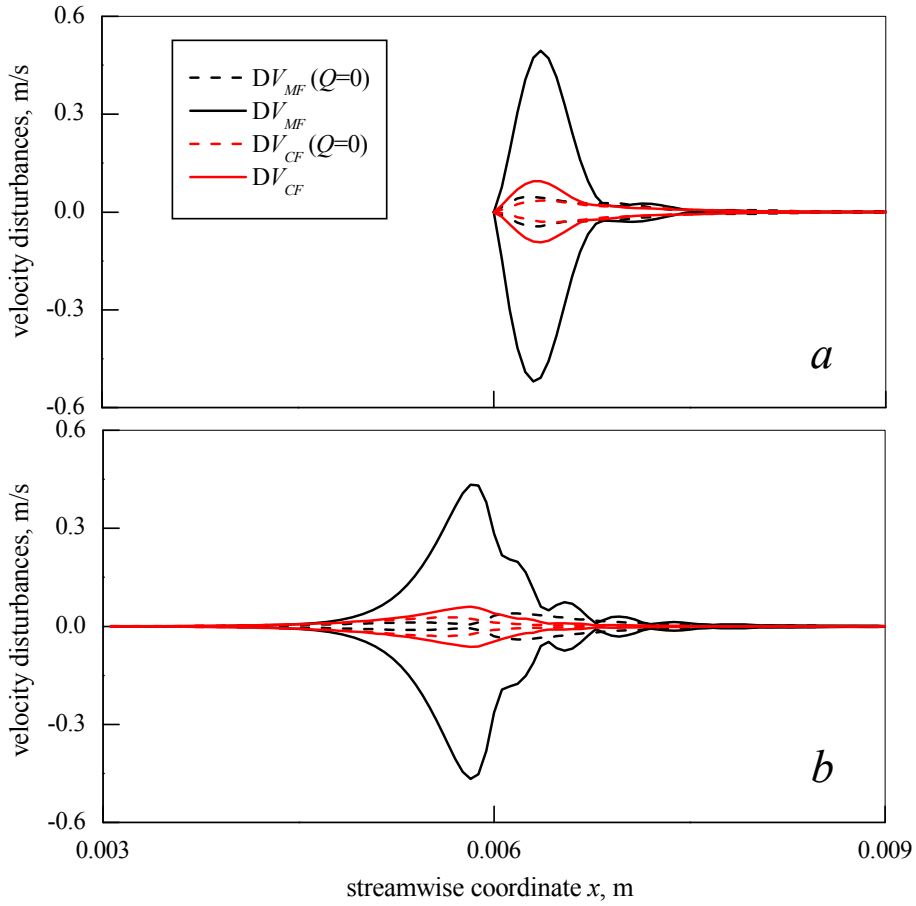

Figure 9: Extremal values of velocity disturbances in variants 1 (*a*) and 2 (*b*).

This appreciable effect of heat impact is explained by the influence of heat release in the boundary layer at a presence of streamwise pressure gradient on streamwise velocity component presenting in equations (2) [19]. Note, the external velocity at the distance $x = 6$ mm reaches $V_e \approx 130$ m/s (see Fig. 3). That is the maximal main-flow velocity disturbances do not exceed 0.4% of the external flow velocity.

The perturbations of the flow vorticity induced by force and heat impact of actuators are the most of interest. The vorticity component oriented along the main-flow streamline $\mathrm{rot}_{MF}\mathbf{V}$ in boundary layer approximation is determined as follows:

$$\mathrm{rot}_{MF}\mathbf{V} = \frac{u_e \mathrm{rot}_x\mathbf{V} + w_e \mathrm{rot}_z\mathbf{V}}{\left(u_e^2 + w_e^2\right)^{1/2}} \equiv \cos\psi\ \mathrm{rot}_x\mathbf{V} + \sin\psi\ \mathrm{rot}_z\mathbf{V}$$
$$\mathrm{rot}_x\mathbf{V} \cong \frac{\partial w}{\partial y}, \quad \mathrm{rot}_z\mathbf{V} \cong -\frac{\partial u}{\partial y} \tag{6}$$

Distributions of the perturbed vorticity oriented along the main-flow streamline at $x = 6.3$ mm for variant 1 (*a*) and $x = 6$ mm for variant 2 (*b*) are shown on Fig. 10. The presented data demonstrate that the force and heat impact of actuators result in three rows of pairs of counter-rotating vortices strongly flattened in vertical direction. The intensities of vortices situated in two rows nearest to the wall are almost equal. The upper row of vortices is significantly weaker. The presented picture of perturbed main-flow vorticity is qualitatively similar to that in the case of solid cylindrical roughness elements [20].

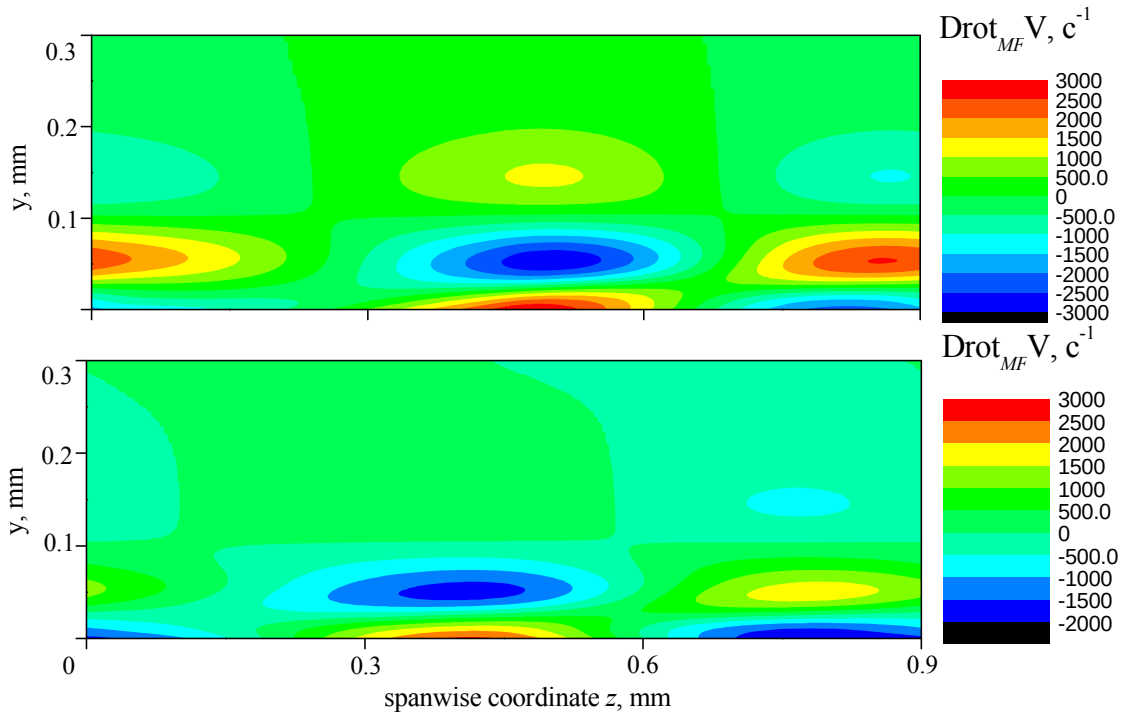

Figure 10: Distributions of perturbed main-flow vorticity in z-y plane for variants 1 (a) and 2 (b).

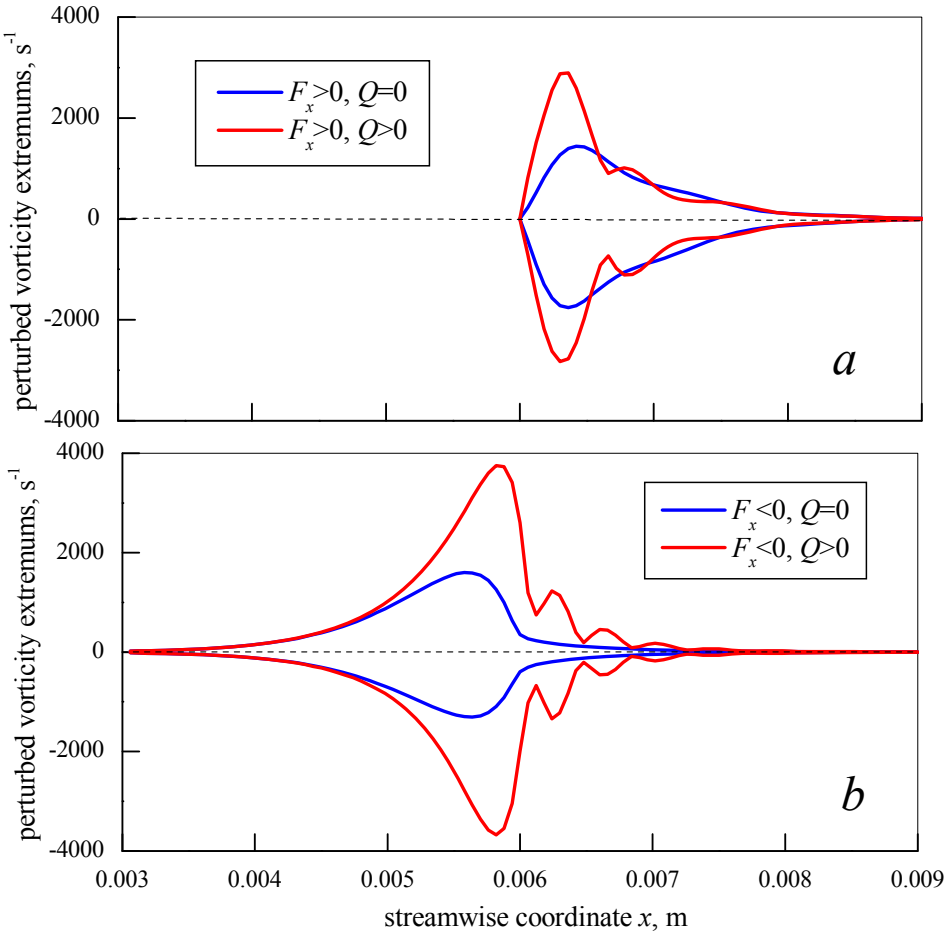

Figure 11: Extremal values of main-flow vorticity perturbation in variants 1 (a) and 2 (b).

The streamwise distributions of extremal values of the perturbed main-flow vorticity are presented on Fig. 11 for force and heat impact and only for force impact. Significant effect of heat release in discharge regions on vorticity perturbation is evident. Moreover the heat impact results in non-monotonic decay of extremal values of perturbations downstream. This phenomenon demands an explanation.

Comparison of Figs. 11 and 6 reveals that very strong vorticity is generated immediately in regions of volumetric force and this vorticity then decays rapidly downstream. For example, the perturbed main-flow vorticity at the distance $x = 8.1$ mm varies in the range $-100 \div 100$ s^{-1} in variant 1 and $-15 \div 15$ s^{-1} in variant 2. But one can notice that the total streamwise length of the domain of actuator influence is a few greater in the case of variant 2. It seems that the problem of critical mode suppression in the considered peculiar case can be solved by incorporation both variants shown on Fig. 1 in single multi-DBD actuator with common buried electrode. The upstream part of this combined actuator in the form of variant 1 acting downstream from $x \approx 6$ mm (see Fig. 5) will prevent to origin of long wave modes and the downstream part in the form of variant 2 acting upstream from $x \approx 9$ mm will excite controlling forced mode.

5 CONCLUSIONS

- Both considered variants of multi-DBD actuator generate three rows of pairs of counter-rotating vortices situated one above another along external streamline. The upper row is significantly weaker as compared to two lower rows.
- Thermal impact of DBD on vortices generation is comparable with force impact.
- High intensive vorticity (the order of 10^3 s^{-1}) is generated immediately in regions of volumetric force and heat sources and then decays rapidly downstream.

REFERENCES

[1] A. Abbas, J. de Vicente, E. Valero, Aerodynamic technologies to improve aircraft performance. *Aerospace Sci. & Technol*., **28**, 100–132, 2013.

[2] D. Arnal, G. Casalis, Laminar-turbulent transition prediction in three-dimensional flows. *Prog. Aerospace Sci.*, **36**, 173–191, 2000.

[3] W.S. Saric, R.B. Carrillo, M.S. Reibert, Leading-edge roughness as a transition control mechanism. *AIAA Paper*, **781**, 1-13, 1998.

[4] W.S. Saric, D.E. West, M.W. Tufts, H.L. Reed, Flight test experiments on discrete roughness element technology for laminar flow control. *AIAA Paper*, **539**, 1-23, 2015.

[5] E.B. White, W.S. Saric, Application of variable leading-edge roughness for transition control on swept wing. *AIAA Paper*, **283**, 1-11, 2000.

[6] J.R. Roth, D.M. Sherman, S.P. Wilkinson, Electrohydrodynamic flow control with a glow–discharge surface plasma. *AIAA Journal*, **38**, 1166-1172, 2000.

[7] D. Schatzman, M. Wicks, P. Bowles, F. Thomas, T. Corke, A parametric investigation of plasma streamwise vortex generator performance. *AIAA Paper*, **824**, 1-10, 2012.

[8] T. N. Jukes, K.-S. Choi, On the formation of streamwise vortices by plasma vortex generators. *J. Fluid Mech*., **733**, 370–393, 2013.

[9] I. Moralev, V. Sherbakova, P. Kazansky, A. Efimov, V. Bityurin, The structure of the dielectric barrier discharge and its effect on the discharge inintiated gasdynamic disturbances. *Proceedings of EUCASS-2015, Report FP EUCASS-357*, Krakow, Poland, 29 June-3 July, 2015.

[10] R. Joussot, A. Leroy, R. Weber, H. Rabat, S. Loyer, D. Hong, Plasma morphology and induced airflow characterization of a DBD actuator with serrated electrode. *J. Phys. D: Appl. Phys.*, **46**, 125204 (12 pp), 2013.

[11] R. J. Durscher, S. Roy, Three-dimensional flow measurements induced from serpentine plasma actuators in quiescent air. *J. Phys. D: Appl. Phys*., **45**, 035202 (9 pp), 2012.

[12] S.L. Chernyshev, A.P. Kuryachii, S.V. Manuilovich, D.A. Rusyanov, V.V. Skvortsov, Attenuation of cross-flow-type instability in compressible boundary layer by means of plasma actuators. *AIAA Paper*, **321**, 1-16, 2013.

[13] D. Dunn, C Lin, The stability of the laminar boundary layer in a compressible fluid for the case of three-dimensional disturbances. *J. Aeronautical Sci.,* **19**, 491–502, 1952.

[14] D.A. Russianov, M.V. Ustinov, A.A. Uspensky, A. Yu. Urusov, Action of multiple-electrodes DBD actuators on the boundary layer: theory and experiment. *Proceedings of EUCASS-2015, Report FP EUCASS-220*, Krakow, Poland, 29 June-3 July, 2015.

[15] N. Benard, A. Debien, E. Moreau, Time-dependent volume force produced by a non-thermal plasma actuator from experimental velocity field. *J. Phys. D: Appl. Phys*. **46**, 245201 (12 pp), 2013.

[16] J. Kriegseis, C. Schwarz, C. Tropea, S. Grundmann, Velocity-information-based force-term estimation of dielectric-barrier discharge plasma actuators. *J. Phys. D: Appl. Phys*. **46**, 055202 (13 pp), 2013.

[17] N. Benard, M. Caron, E. Moreau, Evaluation of the time-resolved EHD force produced by a plasma actuator by particle image velocimetry – a parametric study. *Journal of Physics: Conference Series* **646**. 012055 (4 pp), 2015.

[18] N. Benard, E. Moreau, Electrical and mechanical characteristics of surface AC dielectric barrier discharge plasma actuators applied to airflow control. *Exp. Fluids.* **55**, 1846 (43 pp), 2014.

[19] A.P. Kuryachii A, S.V. Manuilovich, Attenuation of cross-flow-type instability in a 3D boundary layer due to volumetric force impact. *TsAGI Sci. Journal*, **42**, 345-360, 2011.

[20] D.P. Rizzeta, M.R. Visbal, H.L. Reed, W.S. Saric, Direct numerical simulation of discrete roughness on a swept-wing leading edge. *AIAA Journal*, **48**, 2660-2673, 2010.